

In situ alloying of Ti10Mo fused tracks and layers via laser powder bed fusion

Thywill Cephas Dzogbewu^{1,2,*}  and Willie Bouwer du Preez² 

¹ Department of Mechanical and Mechatronics Engineering, Faculty of Engineering, Built Environment and Information Technology, Central University of Technology, Free State, Bloemfontein, South Africa

² Centre for Rapid Prototyping and Manufacturing, Faculty of Engineering, Built Environment and Information Technology, Central University of Technology, Free State, Bloemfontein, South Africa

Received: 10 February 2022 / Accepted: 18 July 2022

Abstract. Optimum process parameters for manufacturing a Ti10Mo alloy for biomedical applications via the laser powder bed fusion (LPBF) process were determined. Fused tracks were produced over a wide range of laser powers and scanning speeds, and layers were fused at varied hatch distances. The samples were analysed for continuity of the fused tracks, melting and distribution of the Mo powder particles in the Ti10Mo alloy layers, surface roughness, homogeneity of Mo in the alloy matrix and microhardness. The analysis revealed that the Mo powder particles melted completely in the alloy matrix with only pockets of Mo concentrations, mostly at the peripheries of the fused tracks due to the pushing effect. Complete melting of Mo in the Ti10Mo alloy matrix was due to the small size (1 μm) of the Mo powder particles used in the current experiment. The addition of Mo enhanced the wetting of the powder bed and prevented a pronounced balling effect. From this study, the parameter sets 150 W, 0.5 m/s and 200 W, 1.0 m/s both at a hatch distance of 80 μm , were obtained as the optimum process parameters. However, the Mo concentrations at the peripheries of the molten pool indicated that further research was required before a ‘completely’ homogenous sample could be manufactured via the LPBF process using elemental powder blends.

Keywords: LPBF / Ti10Mo alloy / fused tracks / fused layers / biomedical applications

1 Introduction

A material with potential to be selected for a biomedical application must fulfill several requirements, such as biocompatibility, corrosion resistance, bio-adhesion (allowing bone ingrowth), favourable mechanical properties (e.g. Young’s modulus similar to that of bone, fatigue strength according to the application), processability (powder metallurgy, casting, deformation, machinability, welding, brazing), affordability (low price) etc. [1–3]. Ti6Al4V came to the fore as the most preferred biomaterial according to the ISO 10993 standard and has been used extensively for load-bearing implants [4–6]. Despite the well celebrated and clinical success achieved with the Ti6Al4V alloy, it has some drawbacks, such as high elastic modulus (100–110 GPa) [7,8], which is about two to four times higher than that of human cortical bone (10–30 GPa) [9]. This mismatch between the implants and the bone tissue leads to incomplete load transfer to the bone [10,11]. This phenomenon is known as stress shielding effect [11].

Apart from the stress shielding effect, it is also reported that the use of aluminium in the Ti6Al4V alloy could cause allergic reactions and the use of vanadium is associated with neurological disorders (such as Alzheimer’s disease) [7]. These observations triggered the search for biometals (alloys) that can offer more suitable biomechanical properties (e.g. lower elastic modulus, similar to bone tissue, to prevent the stress shielding effect) that can enhance osseointegration and without any toxic effects.

As a result, most recent research in the field of implant manufacturing has focused on alloying nontoxic beta stabilizing elements (Mo, Nb, Ta, Zr and Sn) with Ti [1]. The Ti-Mo binary alloys have been the subject of several studies due to their unique mechanical properties and corrosion resistance, β phase predominance and non-cytotoxic behaviour. This is because molybdenum is nontoxic and is considered as the most preferred β -stabilizing element. It is able to stabilize β -phase with low solute concentrations [11]. The molybdenum equivalent theory is normally used to determine the amount of Mo concentration of the alloying elements that can stabilize the β phase. It was determined that from 10 wt.% Mo the β phase is already reached [12].

* e-mail: tdzogbewu@cut.ac.za

Ho et al. [12] were one of the first in the 1990s to investigate the suitability of Ti-Mo alloys for biomedical applications using the conventional method of manufacturing (casting). The authors varied the Mo content from 6 to 20 wt.% and reported that the Ti-Mo alloy demonstrated low elastic modulus (<80 Gp) and it was a potential candidate for dental material. Chen [1] investigated the microstructure and biomechanical properties of the binary Ti-Mo alloys with molybdenum contents ranging from 5% to 20% (mass fraction) and reported that the Ti with 10% Mo (Ti10Mo) was the most ideal for biomedical applications. Other researchers also investigated the suitability of the Ti-Mo binary system for biomedical applications with 10 wt.% Mo and reported low elastic moduli (23–40 GPa), no cytotoxicity and preferential properties for biomedical applications as compared to Ti6Al4V [13–15]. Despite these confirmations of low elasticity, non-toxicity, preferential biomechanical and biochemical properties of the Ti-Mo alloy, the processing of the Ti10Mo alloy via the conventional methods (casting, forging, sheet forming, extrusion, etc.) was very difficult [16,17]. This is because Mo is a refractory metal with a high melting point [18]. The addition of Mo to Ti increases the melting point of the alloy making the processing of the material very difficult [16,19]. As a result, the conventional methods of manufacturing could not be used to produce the alloy without defects (porosity, shrinkage, inhomogeneous microstructures) [17].

According to Jablovkov et al. [19], the Ti-Mo alloys are generic alloys that have been around for a long time, however, unlike the Ti6Al4V alloys that have gained wide applications, the Ti-Mo alloys could not find wide industrial applications. This is due to “the physical metallurgy of the alloy and the inability of the then-current reactive metals melting and processing machinery to handle this unusual binary alloy” [19]. The high melting point of the alloy makes it difficult to use the conventional methods to produce the alloy. There is a need to use an alternative efficient method/s to produce the alloy without defects to promote its wider industrial application.

Additive manufacturing (AM) technology is gradually attaining maturity and being used to produce end-user products [6,20–22]. The technology could be used to produce biomedical objects monolithically with tailored geometrical configurations as opposed to the conventional methods [23,24]. AM technology, such as laser powder bed fusion (LPBF) could be used to in-situ alloy different elemental powders to produce intricate (biomimetic) 3D objects with tailored biomechanical properties without using the pre-alloyed powders, which are normally used for LPBF processes [25,26]. The approach of in-situ alloying of different elemental powders without depending on pre-alloyed powders, would lead to cost reduction in the final product, since the production of pre-alloyed powders is a capital intensive process [27].

Other researchers touted the capacity of other advanced manufacturing technologies, such as the electrical discharge machining (EDM) method, which is a non-conventional process normally used to machine hard materials into intricate shapes [28,29]. The EDM technology could certainly be used to produce Ti-based alloy components with intricate shapes for biomedical

applications [30]. However, unlike the LPBF manufacturing process, which is considered a monolithic additive manufacturing process, for EDM the traditional methods such as casting, vacuum arc remelting etc. are required to produce the Ti-based alloy prior to machining (subtractive manufacturing) the workpiece into the required intricate shaped. Such an approach of depending on the classical methods to produce the Ti-based alloy components prior to machining could not yield the desired results [19]. As explained by Jablovkov et al. [19] and Khanna et al. [31], the conventional methods of producing the Ti-based ingot required remelting to homogenise the alloy. The remelting process could lead to carbon and oxygen contamination of the product prior to the EDM machining [19]. As a result, LPBF which does not depend on any prior conventional methods, might be the most ideal technology to be used to produce the Ti-xMo alloy with the required properties for biomedical applications.

Therefore, the current research, seeks to determine process parameters that could be used to produce the Ti10Mo alloy in near-net shapes. Production of the Ti10Mo alloy with complex geometrical characteristics (near-net shapes) would enhance its technical and functional applications, leading to widespread industrial applications. The LPBF process is a layer-wise building process and single tracks are the basic unit building blocks [26]. It is the side-by-side arrangement of the fused tracks that results in a single layer, and it is the superposition and fusion of the layers that result in a 3D object [32]. To produce fully dense 3D objects from the Ti10Mo powder material, optimal process parameters that could produce quality fused tracks and layers are paramount. Spears and Gold [33] stated that there were more than 50 process parameters influencing the mechanical properties of LPBF products. However, it could be inferred from the hierarchical principle of Yadroitsev et al. [34] that laser power, scanning speed and hatch distance were the principal process parameters having a direct decisive effect on the final 3D components produced by the LPBF process. Therefore, the current research determined the laser power, scanning speed and hatch distance that could be used to produce Ti10Mo fused tracks and layers. Determination of the optimum process parameters that could be used to produce the Ti10Mo fused tracks and layers would pave the way for the possible production of dense Ti10Mo 3D structures without defects, which could promote the widespread industrial application of the Ti10Mo binary alloy.

2 Materials and methods

Spherical argon atomised Ti (CpTi, grade 2) and plate-like Mo powders procured from TLS Technik GmbH were used for the studies (see Fig. 1). The chemical composition of the Ti as analysed by the supplier, was presented in wt.%: Ti (bal.), O (0.17), Fe (0.062), C (0.006), H (0.002), N (0.012) and the particle size distribution was expressed as: $d_{10} = 11.6 \mu\text{m}$, $d_{50} = 24.6 \mu\text{m}$, $d_{90} = 38.4 \mu\text{m}$. The average particle size of Mo was $1 \mu\text{m}$ and the purity was 99.9%. In the mixing process 90 wt.% of Ti was mixed with 10 wt.% of Mo in a 3D Turbula[®]-like mixer, driven by a

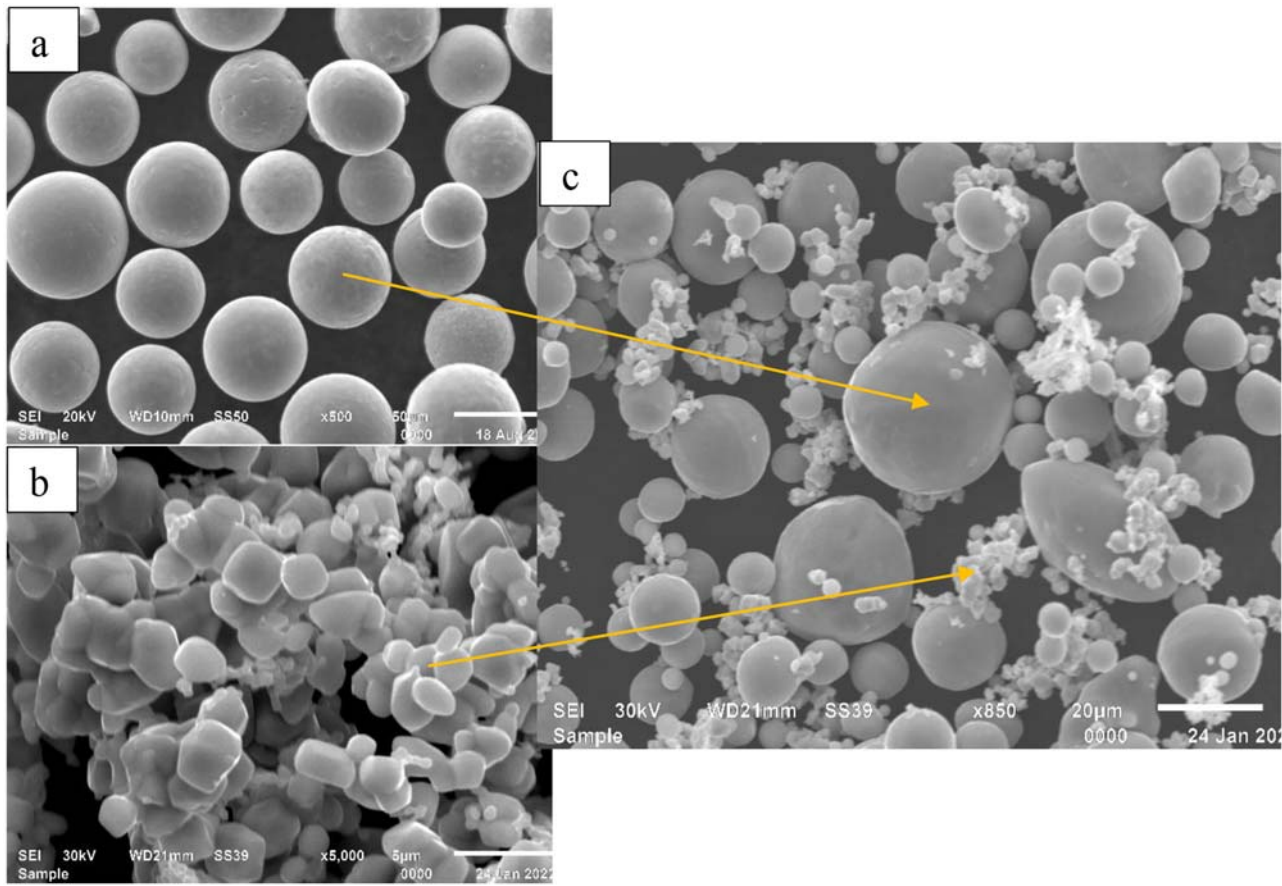


Fig. 1. SEM images of the powders: (a) Ti powder, (b) Mo powder, (c) Ti10Mo powder blend.

SEW-Eurodrive motor and Movitrac controller for 30 min at 150 rpm. The resultant 90 wt.% Ti and 10 wt.% Mo powder mixture is referred to as Ti10Mo powder blend throughout the article. It was dried in an oven for 12 h at 80 °C and stirred at 30 min intervals to enhance the flowability of the powder during the LPBF process.

An Electro-Optical Systems GmbH (EOS) EOSINT M280 direct metal laser sintering (DMLS) machine was used for the studies. The machine was equipped with a 400 watt Yb-fibre laser and operated at a laser spot size of 80 μm. Argon was used as inert gas during the build process. CpTi, grade 2 plate was used as the substrate and the powder layer thickness was 50 μm. Fused tracks were produced over a wide range of laser powers (50–350 W) and scanning speeds (0.08–3.2 m/s). Three fused tracks were produced for each combination of laser power and scanning speed. The optimum parameters obtained from the top and cross-sectional views of the fused tracks were used to produce layers at varied hatch distances of 80 μm, 90 μm and 100 μm.

The cross-sections of the fused tracks and layers were subjected to standard Struers [35] metallurgical sample preparation protocol (grinding with 320 SiC papers, polishing with diamond suspensions of 9, 3 and 1 μm sizes) and etched with Kroll's reagent. For analysing the top view and cross-sectional view of the fused tracks and layers, optical and scanning electron microscopy was used.

The geometrical characteristics of the fused tracks, their width (W), height (H) and penetration depth (D), were analysed as demonstrated elsewhere [36]. The surface roughness of the fused layers was measured using a Surftest SJ-210 portable surface roughness tester procured from Mitutoyo America Corporation. Microhardness tests of the samples were conducted on polished cross-sections perpendicular to the building direction at 200 g loading for a holding time of 15 s. For statistical purposes, 20 measurements were taken for each cross-section.

3 Results and discussion

Formation of continuous stable tracks is a prerequisite for successful manufacturing of a 3D object through the LPBF process. Stability of the geometrical characteristics of each fused track and good adhesion (cohesion) between the layers are critical factors for structural integrity and high-quality manufacturing of LPBF components. The stability of the geometry of the fused tracks is governed by the energy parameters of the laser radiation [37,38], substrate system phenomena (absorption, radiation and heat transfer, reflection, fluid flow driven by surface tension gradients and mass transfer within the molten pool, phase transformations, chemical reactions etc.) [39], granulomorphometric characteristics of the powder (powder particles size

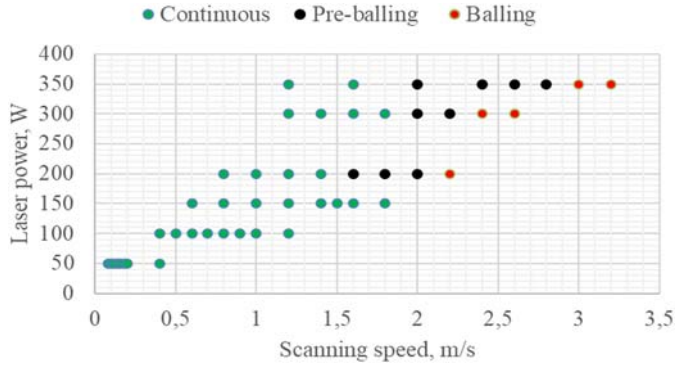


Fig. 2. Classification of the nature of the fused tracks.

and distribution, powder bed density) [40,41], thermo-physical properties of the powder (absorptivity, specific heat capacity, thermal conductivity, density, coefficient of thermal expansion, phase transformation temperatures) [40], peculiarities of the powder deposition and spreading [41] and machine-based conditions [33]. The above-mentioned parameters determined the hydrodynamic movement of the molten pool [10,42].

3.1 Top surface analysis of the fused tracks

For the current experimentation, single tracks were produced over a wide range of laser powers and scanning speeds (varying laser energy density). The threshold parameters that produced continuous tracks are presented in Figure 2 and the morphology of the tracks are presented in Figure 3. It could be observed that at all the lower laser powers (50–150 W) and low scanning speeds (<2 m/s) all the tracks were continuous (Fig. 2).

According to the Plateau-Rayleigh effect [43], “a free liquid cylinder is unstable if the ratio of its length L to diameter W exceeds π (unity or 1)”. This implies that the Ti10Mo molten metal cylindrical liquid would produce continuous tracks if the ratio of the width of the tracks to the diameter <1 and discontinued tracks if the ratio >1. The width of the fused track is generally dependent on the laser energy input (P/V) [38]. At a higher laser input the temperature in the molten pool increases. A high fusing temperature would produce a large liquid phase with low viscosity which would lead to a prominent flow of the molten liquid (enlarged liquid phase curvature). The large liquid phase produces fused tracks with a large width, while low fusing temperature produces tracks with a smaller width. It could be postulated that for the current experiment the width of the tracks produced at low fusing temperatures correspond to the diameters of the fused tracks resulting in width to diameter ratios <1, while the width to diameter ratio of tracks produced at higher operating temperatures resulted in width to diameter ratios >1. This could be attributed to the fact that at a higher input temperature the convective flow (Marangoni effect) [44] within the molten pool increases. The high convective melt flow coupled with the rapid solidification of the hydrodynamic capillary fluid could trigger Rayleigh–Plateau capillary instability [45]

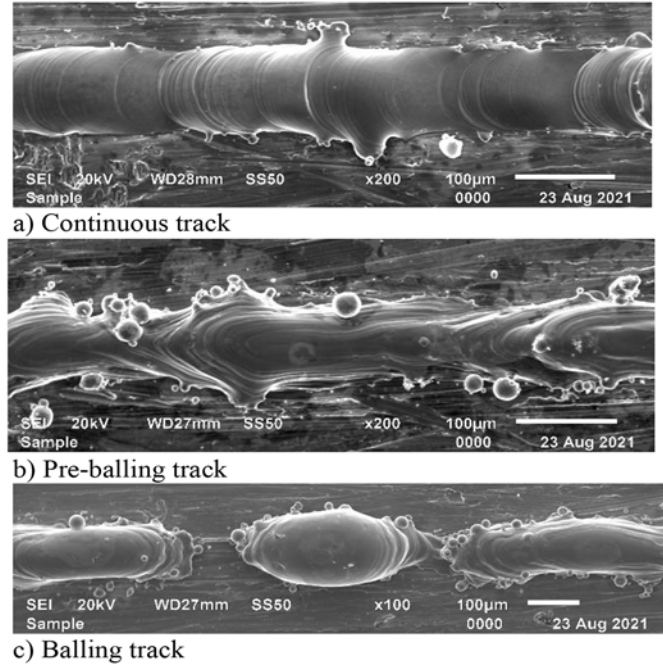


Fig. 3. Geometry of fused tracks from the top view. (a) 150 W, 0.5 m/s; (b) 200 W, 1.6 m/s; (c) 200 W, 2.2 m/s.

leading to the formation of discontinued tracks at high input temperatures. The operating temperature of laser melt pool was computed by Fischer et al. [46] as:

$$\Delta T = \frac{2AE}{K} \sqrt{\frac{k_{th} T_p}{\pi}} \quad (1)$$

where A is the laser absorption coefficient, E is the laser beam energy, k is the thermal conductivity, k_{th} is the heat diffusivity and T_p is the laser irradiation duration.

A high laser power induces a high E , resulting in a higher operating temperature of the molten pool [47]. For the current experiment, discontinued tracks were formed at high laser powers (300 and 350 W) and high scanning speeds (>2.0 m/s) (Figs. 2 and 3b,c). The discontinued tracks could be pre-balling (long beads – Fig. 3b) or balling (Fig. 3c) depending on the nature of the solidified molten front [40,41]. The molten front basically depends on the wettability of the powder and the underlying substrate by the molten liquid. For the laser melting process, wetting could be defined as the spreading of the molten liquid on the substrate (the previously solidified layer) instead of balling up on the surface of the substrate. The adhesive force between the solid and liquid is greater than the cohesive force of the liquid during the laser melting process [34]. This phenomenon makes it possible for the molten liquid to wet the powder bed. The wettability of the powder and the underlying substrate also depends on the density of the powder bed [40]. For the current experiment, the density of the powder bed improved due to the small particle size of Mo. The 1.0 μm Mo powder particle would fill the gaps between the 45 μm Ti powder in the powder bed. Due to the high density of the powder bed, most of the fused tracks

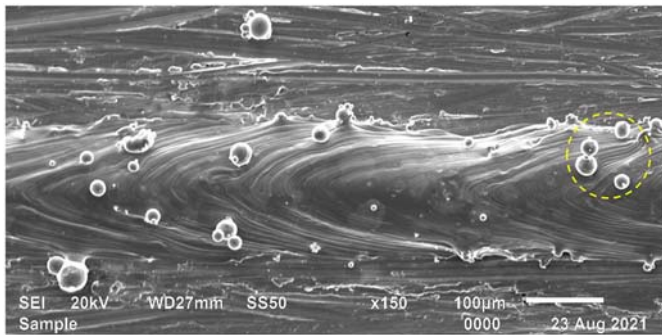


Fig. 4. Spattering (satellites) on the melt pool.

were continuous and the discontinuous tracks were mostly long beads (200 W, 1.6–2.2 m/s; 300 W, 2.0–2.6 m/s and 350 W, 2.0–2.8 m/s) (Figs. 2 and 3b). Only tracks produced at a laser power of 200–350 W at scanning speeds above 2.2 m/s formed balls (Figs. 2 and 3c). Previous research by the authors with Mo powder particle size of 45 μm could not yield continuous tracks at most of the laser powers and scanning speeds [38,42]. Das [40] also reported that ‘balling becomes very pronounced if the molten liquid fails to wet the powder or the plate’. Thus, wetting ridges could affect the behaviour of the cylindrical molten fluid and the spreading of the molten liquid on the substrate [48]. However, because of the high degree of wettability of the powder and the underlying substrate due to the improved powder density of the powder bed, the balling effect much less pronounced in the current experiment. This observation confirmed that the granulometric characteristics of the powder size have a significant effect on the geometry of the solidified fused tracks.

3.1.1 Spatter particles

Spatter particles, which are commonly known as satellites [34], are observed on the surfaces and edges of the fused tracks (Fig. 4—the yellow dotted circle).

As the laser beam traverses the powder bed, it does not only melt the powder positioned directly under the laser spot, but also powder particles in the peripheries of the laser beam. Melting of the powder particles at the borders of the laser beam occurs due to scattering of the laser radiation, capillary phenomena, conduction through the substrate and neighbouring particles [49]. The melting of the powder particles at the edge of the cylindrical molten pool occurs towards the end of the solidification process [42]. As a result, there is not sufficient energy to melt the powder particles completely and incorporate them into the bulk material. Consequently, the partially melted powder particles stick to the edges of the fused tracks as spatter particles [25]. In addition, spatter particles could form due to the diving of the molten liquid ahead of the laser spot similar to the movement of a boat through water [50]. As a boat moves through water, bow waves develop in front of the advancing motion of the boat. Similarly, during the laser melting process, the molten liquid builds up ahead of the laser spot and could deposit onto the powder bed as

spatter particles [49]. Due to the rapid solidification process during LPBF, the spill-off liquid solidifies on the surface of the cylindrical melt pool as spatter particles.

For the current experiment, it appears that there are no spatter particles on the edges and surfaces of tracks fused at lower laser powers (50–150 W) and scanning speeds <1.4 m/s (Fig. 3a). It was noted that the number of spatter particles increased with increasing laser power and scanning speed on the surfaces and edges of the fused tracks. At a lower scanning speed, the dwell time of the laser beam at a particular spot on the powder bed is longer. Due to the longer dwell time (slower movement) of the laser beam, the powder particles at the peripheries of the laser spot have greater chances of being melted completely and incorporated into the bulk material, as compared to high scanning speeds where the dwell time of the laser beam on a particular spot on the powder bed is shorter. As result, the number of spatter particles on edge of the solidified molten pool decreases with decreasing scanning speed. Secondly, at a high laser power the operating temperature in the molten pool increases (Eq. (1)). Higher melt temperature implies higher convective melt flow (Marangoni effect) [44]. This higher convective melt flow at a higher operating temperature leads to a higher probability of the molten liquid being deposited ahead of the advancing laser spot. As result, there are more spatter particles at the surfaces of the solidified fused tracks at higher laser powers than at lower laser powers.

Partial melting of the powder particles at the border of the laser spot and the deposition of the molten liquid ahead of the laser spot could provoke pore formation in 3D parts and increase surface roughness [51]. Partial melting of the Ti10Mo powder in the peripheral zone of the laser spot is the main cause of the denudation effect [52]. This results from the diminishing of the amount of power available to produce the next fused track, due to the partial melting of the powder particles at the borders of the laser spot.

3.1.2 Track width (W)

Because the width (W) of the fused tracks determines the hatch distance (distance between neighbouring single tracks) that should be used, the widths of the single tracks in the current experiment were measured. From Figure 5, it was observed that the width of the tracks decreased with increasing scanning speed at the same laser power.

As the scanning speed increased the laser energy density decreased (Fig. 5), causing the operating temperature in the molten pool to reduce. The reduction in the molten pool temperature produced fused tracks with reduced liquid phase curvature, while higher operating temperatures produced fused tracks with broad liquid phase curvature. Consequently, the widths of the fused tracks decreased with increasing scanning speed (Fig. 5). Generally, the width of the tracks increased with increasing laser power. However, the widths of the tracks at 200 W were greater than the width of the tracks at 300 W. Since the discontinuity of the tracks increases with increasing laser powers and scanning speeds (Fig. 2), this anomalous observation of the width of the tracks produced at 200 W wider than tracks produced at 300 W could be attributed to

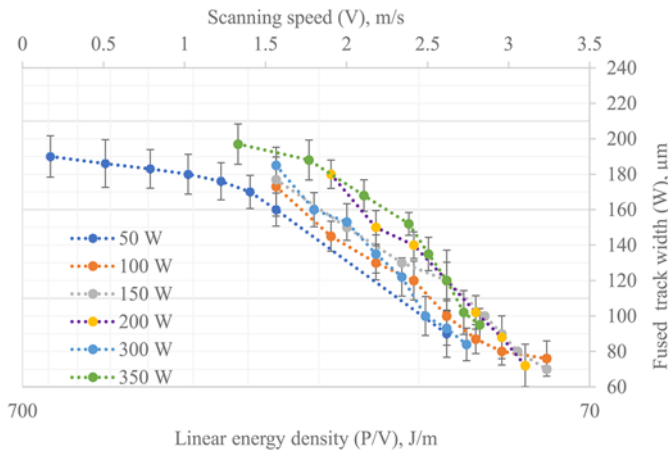


Fig. 5. Effect of linear energy density (P/V) on the width of the fused tracks in relation to scanning speeds.

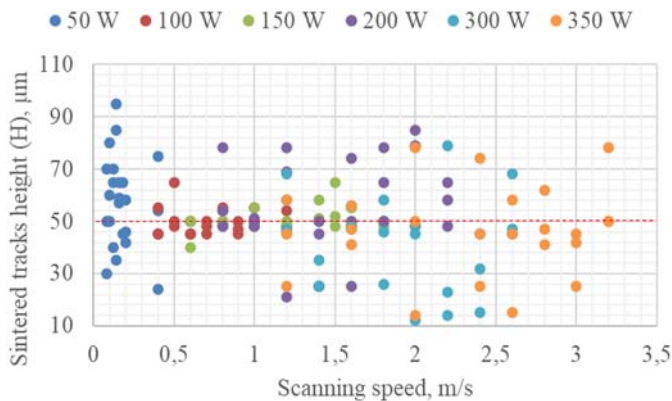


Fig. 6. The height of fused tracks versus the scanning speed.

the difficulty of measuring discontinuous tracks. Ten measurements were taken per track. Continuous measurements of a series of discontinuous tracks could affect the result of the width of the tracks. This anomalous observation also confirmed the non-linearity of the LPBF process as reported elsewhere [34,36,53].

3.1.3 Track height

The height (H) of the tracks, which is directly related to the powder layer thickness ($50\ \mu\text{m}$) deposited on the substrate, was also investigated. Due to the Gaussian profile of the laser beam, a temperature gradient develops within the molten pool. As mentioned earlier, the temperature gradient triggers a recirculating flow within the molten pool (Marangoni effect) [44]. The recirculating flow (waves) within the molten pool amplifies the oscillation of the pool surface, leading to ripple formation as the molten metal solidifies [54]. According to Qiu et al. [54], the hydrodynamic movement within the molten pool causes the molten pool to move in a dispersed and random way leading to track heights that differ from the thickness of the initial deposited powder layer (Figs. 6 and 7).

Körner et al. [41] also emphasized that the formation of the stochastic (irregular, corrugated) melt track heads (height) was due to the complex melt flow behaviour

governed by laser beam absorption, surface tension, viscosity, gravity and capillary effects. For the current experiment, there was no linear relationship between the heights of the fused tracks and the process parameters (Fig. 6). Although the initial deposited powder layer thickness was $50\ \mu\text{m}$, the final track heights varied randomly with no relationship of the track heads with the scanning speed and the laser power. This phenomenon could possibly lead to irregular powder deposition, which could cause uneven laser absorption during subsequent scanning.

3.2 Cross-sectional analysis of the fused tracks

The penetration depth (D) (the extent to which the laser beam melted the substrate) [25] of the fused tracks into the substrate was also investigated, since the LPBF process is a layer-wise building process. The penetration depth of the fused tracks into the substrate determines the metallurgical bonds between the layers. The mode of laser-matter interaction in the powder bed is generally classified into the conduction mode and the keyhole mode, which is dependent on the laser energy density [55]. At a relatively low laser energy density (Fig. 4) the laser energy melts the powder particles locally and the heat transport occurs mainly via conduction and convection within the molten pool, which is denoted as conduction mode (Fig. 8c). The keyhole mode occurs at a higher laser energy density, where the laser energy is high enough to melt the powder in the powder bed and also ‘drill’ into the substrate (previously solidified layers) (Fig. 8d). This causes a dense vapour plume that consists of a cluster of atoms, molecules, ions and electrons, which triggers a recoil momentum on the molten material to form a cavity in the solidified molten pool [39]. Since there is no further deep melting below the surface of the substrate during the conduction mode, fused tracks that are formed in conduction mode normally have a U shape profile (Fig. 8c) and keyhole penetration has a V shape profile (Fig. 8d). Because the heat input during conduction mode is under control, tracks that demonstrate conduction mode of penetration are generally not prone to defects (porosity, crack and spatter) [36].

For the current experiments, tracks produced at laser power 100 W, 0.5 m/s and 200 W, 1.0 m/s demonstrated conduction mode profile (U shape – optimum process parameter), while the combination of the other process parameters could not yield the desired results (see Fig. 9).

A conduction mode is achieved when the ratio of half the width of the track to its penetration depth equals unity (1). The penetration depth divided by track half width ratio versus the laser scanning speed is shown in Figure 10.

In this figure the ratio $0.5W = D = 1$ is given by the purple dotted line [10,56]. From Figure 10, it is clear that the half width to the penetration depth ratio of tracks produced at 100 W, 0.5 m/s and 200 W, 1 m/s equals 1. Therefore, these process parameters (Fig. 3c) are ideal for producing 3D objects without defects. Combinations of process parameters that are below the threshold line (the purple dotted line) would produce tracks with no or insufficient penetration, while combinations of process parameters above the threshold line would produce tracks

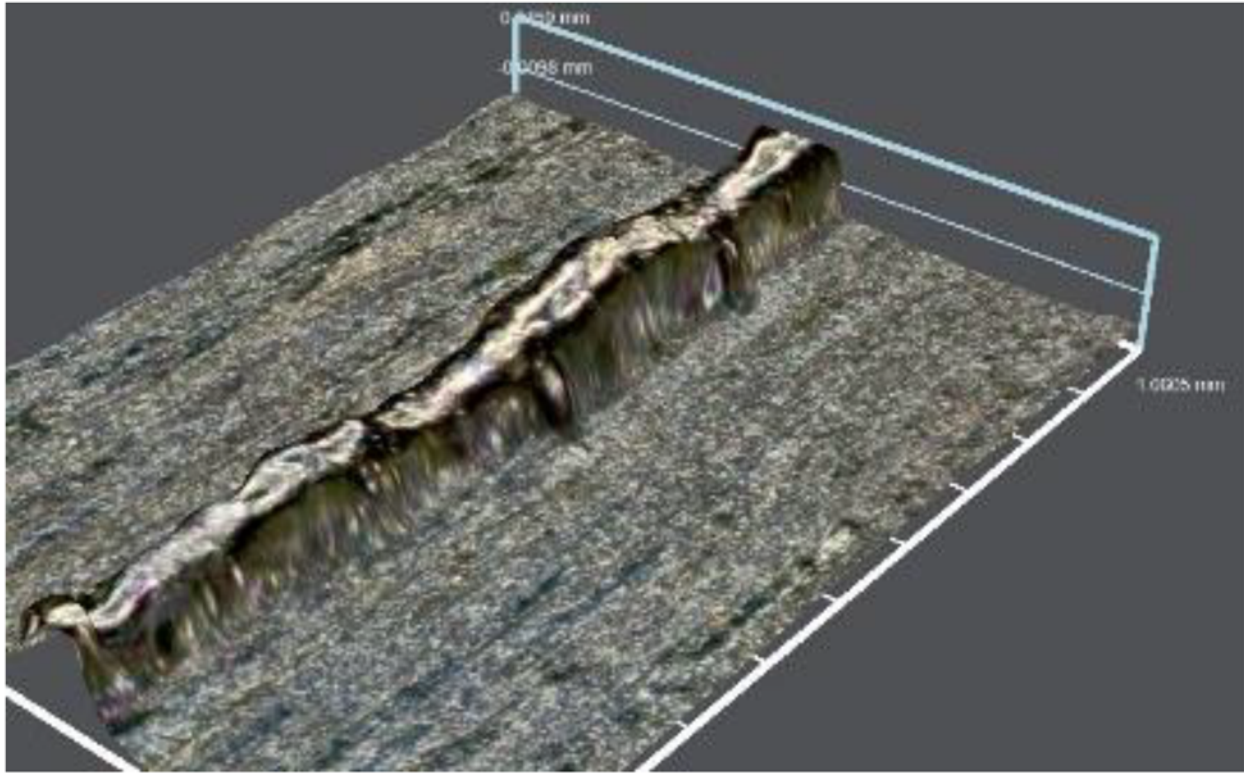


Fig. 7. A micrographic image of the irregularity of the track heights.

in the keyhole mode. Therefore, there seems to be a threshold for sets of process parameters that produce fused tracks in the conduction mode, keyhole mode and shallow mode of penetration.

Tracks that demonstrated keyhole mode formation could lead to pore formation in the final products while no or insufficient modes of penetration could lead to interlayer pores (Figs. 8a and b). In the latter case, the laser energy density is not enough to melt the powder particles and penetrate the substrate sufficiently to form the desired metallurgical bond.

Rai et al. [57] postulated that the threshold for transition from the conduction mode to the keyhole mode is $T_{\max} \geq T_b$ where T_{\max} is the maximum operating temperature of the molten pool and T_b is the boiling temperature of the powder particles. Bäuerle [58] stated that for a Gaussian laser beam of spot size d , the maximum operating temperature T_{\max} of the molten pool, could be estimated as

$$T_{\max} = \frac{\sqrt{2}AId}{k\sqrt{\pi}} \tan^{-1} \frac{\sqrt{2Dt}}{d} \quad (2)$$

where A is the absorption coefficient of the material, I is laser intensity, d is the laser spot size, k is the thermal conductivity of the molten material, D is thermal diffusivity of molten material, and t is the interaction time between the laser beam and the constituent powder.

King et al. [55] gave a precise description of switching from one mode of the laser melting process to another, according to the LPBF process parameters based on the

interaction time between the laser beam and the powder, ($t = \frac{d}{v}$), in terms of the normalised enthalpy ($\frac{\Delta H}{h_s}$).

$$\frac{\Delta H}{h_s} = \frac{AP\sqrt{D}}{KT_m\sqrt{\pi V}d^3} \geq \frac{\pi T_b}{T_m} \quad (3)$$

where, $h_s = \frac{KT_m}{D}$ is the enthalpy at melting and T_m is the melting point.

Based on the detailed work done by King et al. [55], it could be observed that the threshold for transition from the conduction mode to the keyhole mode is directly determined by the applied laser power, scanning speed and beam size diameter. Because the beam size diameter (80 μm) was constant in the current experiment, it could be concluded that the scanning speed and laser power were the determining factors of the various laser melting profiles in the current experiment.

The threshold normalised enthalpy for the current experiment was $\frac{\Delta H}{h_s} \sim 45 - 70$ (Fig. 10; the range between the red dotted lines – line A and line B).

Since the elemental powder blend was made up of 90 wt.% Ti, the thermophysical properties of the precursor powder (Tab. 1) was used for the calculations.

Any value above the enthalpy threshold values would produce deep penetration (Fig. 10—the purple dotted circle) and values below the threshold value would produce shallow penetration. However, as opposed to the theoretical observation, deep penetrations were observed below the enthalpy threshold values (Fig. 10; the black dotted oval). In the range of the threshold values $\frac{\Delta H}{h_s} \sim 45 - 70$,

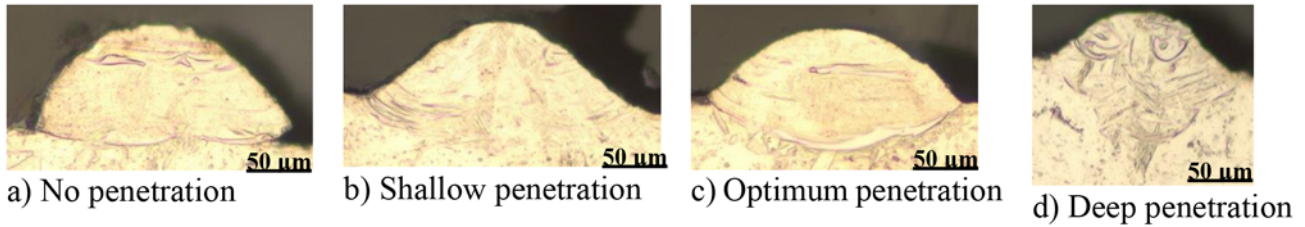


Fig. 8. Cross-sectional view of the geometry of fused tracks.

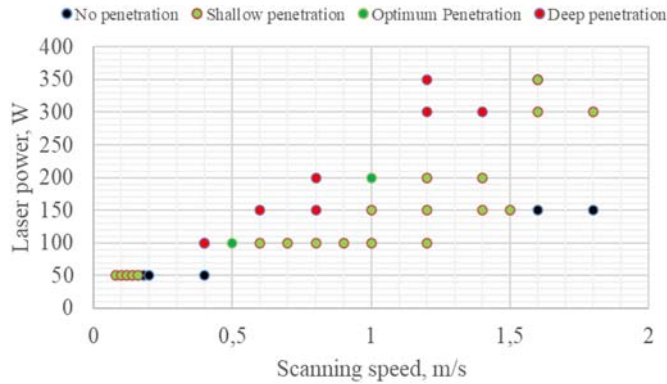


Fig. 9. Penetration depth of fused tracks.

there are penetration depths below and above the purple dotted line, indicating that within the threshold enthalpy range a transition can take place from shallow penetration to conduction and deep penetration. King et al. [55] noted that the normalised enthalpy theory scaling is lacking some physics and failed to account for the additional physics that exist in the keyhole formation process. However, for the current experiment the use of an elemental powder blended could also contribute to the deviation from theoretical expectations. This is because the normalised enthalpy theory was based on pre-alloyed powders. The 10 wt.% Mo could change the laser-matter interaction and the mechanical properties of the material significantly, just like 0.5 wt.% of C can change the properties of steel [61].

These observations reveal that the LPBF process is non-linear, and the practical observation does not always conform with theoretical expectations. This might be the reason that, despite the increase in computation power, leading numerical investigations to predict the thermal fields (penetration profiles) during the LPBF process is still at the research stage. Optimum process parameters are currently still determined via experimental methods. Numerical simulations are only used as optimization algorithms for the selection of the range of initial process parameters that are subsequently investigated experimentally to determine the optimum process parameters. This challenge arises due to the numerous LPBF process parameters/conditions (laser input parameters, machine-based conditions, power particles characteristics, laser-matter interaction on the powder bed – which includes absorption, conduction and convection, reflection,

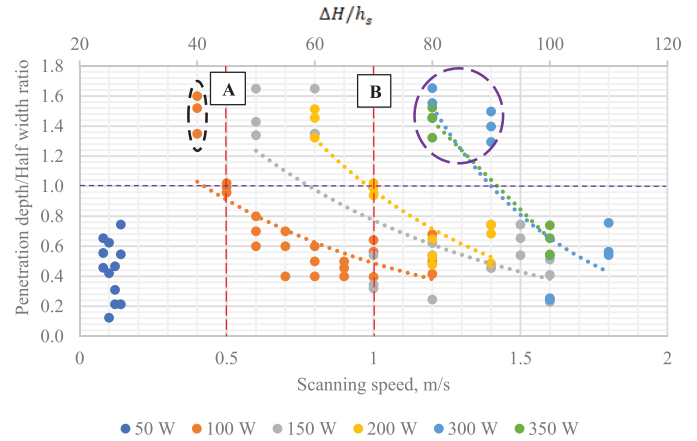


Fig. 10. Normalised enthalpy.

evaporation and emission of material, radiation phenomena, chemical reactions, fluid flows and solidification). All these interactions make it very difficult to predict the geometry/profile of the fused tracks using only numerical simulations.

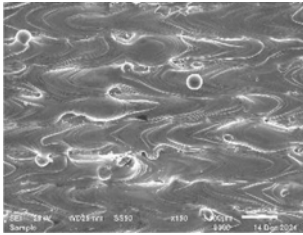
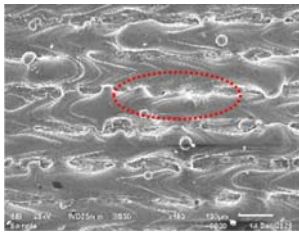
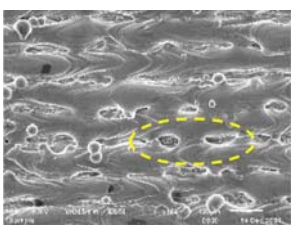
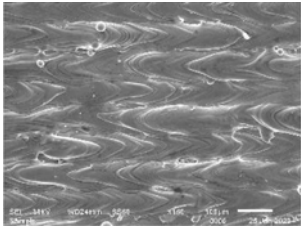
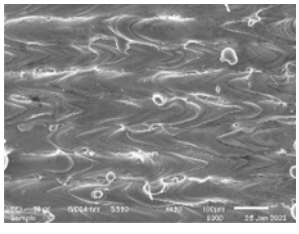
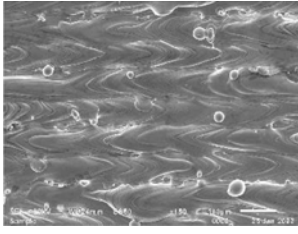
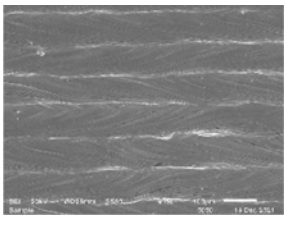
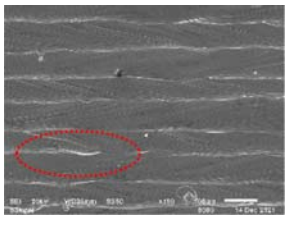
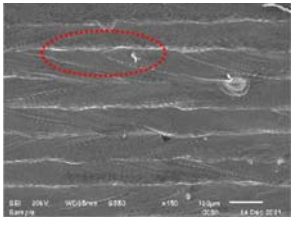
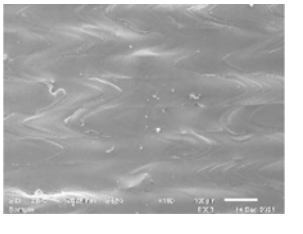
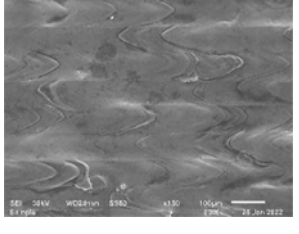
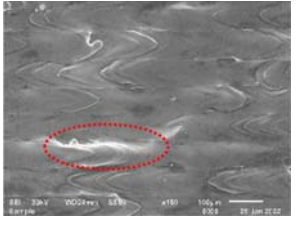
3.3 Top view of the fused layers

The side by side overlapping of the fused tracks resulted in a single layer and the superposition of the layers would result in the production of a 3D object. The surface morphology of the layers generally depends on the geometrical characteristics of fused tracks, scanning strategy and hatch distance, which shifts between tracks in the plane of the laser beam. The fused layers were examined at various hatch distances (80 μm , 90 μm , and 100 μm) to determine the optimum hatch distance for producing a 3D structure without porosity. It was observed that at all the hatch distances the fused tracks seem to overlap and there were pockets of Mo concentration, especially at the borders of the tracks, as shown in Table 2, where the red dotted ovals were drawn around the white Mo concentrations. However, micropores could be observed on the surfaces of layers produced at 100 μm (Tab. 2, Single scan – the yellow dotted oval). There were fewer satellites on the surfaces of layers produced at 80 μm hatch distance, as compared to layers produced at 90 and 100 μm hatch distances. The size of the satellites at 100 μm hatch distance seemed larger than the satellites at 80 and 90 μm hatch distances.

Table 1. Thermophysical properties of Ti.

	Values [59,60]
Thermal conductivity, k ($\text{Wm}^{-1}\text{K}^{-1}$)	17
Boiling point, T_b (K)	3 560
Melting point, T_m (K)	1 941
Absorption coefficient, η	0.77
Thermal diffusivity, D (m^2s^{-1})	7.15×10^{-6}

Table 2. Surface morphology of the layers with different scanning strategies and hatch distances.

Process parameters	Single scan		
	80 μm	90 μm	100 μm
100 W, 0.5 m/s			
200 W, 1.0 m/s			
100 W, 0.5 m/s		Rescan	
			
200 W, 1.0 m/s			

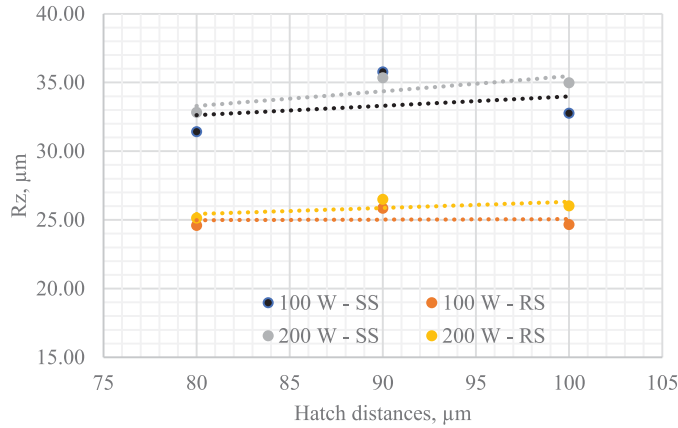


Fig. 11. Surface roughness (R_z) of the layers with different scanning strategies (SS = single scan, RS = Rescan).

The presence of the micropores at the highest hatch distance could be due to the denudation zone effect [34], resulting from the large size of the hatch distance (100 μm). As noted earlier, the zone of powder consolidation diminishes with subsequent scanning, because the laser does not only melt powder particles directly under the laser spot, but also powder particles in the periphery of the laser beam. Therefore, the powder volume involved in the laser melting process in a subsequent scan is reduced [26]. The width of the track's ranges between 70 and 200 μm (Fig. 5), hence there should theoretically not be a micropore at any of the hatch distances. It is generally accepted that the selected hatch distance values should not be greater than the average width of the fused tracks to ensure sufficient overlapping between neighbouring tracks [26,36,38]. The presence of the micropores at 100 μm hatch distance confirms that the denudation effect could lead to interlayer pores [26]. However, the layers produced at 80 μm hatch distance have a higher degree of overlapping, thereby eliminating the denudation zone effect as compared to the layers at 90 and 100 μm hatch distance. The higher degree of overlapping also reduces the number of satellites on the surfaces produce at 80 μm as compared to the 90 and 100 μm hatch distance. Since satellites are formed mainly by melt spattering and partial powder melting in the peripheral zone of the laser spot, at a smaller hatch distance the possibility of remelting the satellites on the surface and the edge of the fused tracks is higher. As a result, there are fewer satellites on the surface of layers produce at 80 μm hatch distance as compared to layers at 90 and 100 μm. Hence the 90 and 100 μm hatch distances between the tracks in the plane of the laser beam scanning is less desirable as compared to the 80 μm hatch distance.

3.3.1 Surface quality of the Ti10Mo alloy matrix layers

Despite the well-celebrated advantages offered by the LPBF process, it is well documented that the surface quality of LPBF products is one of its main drawbacks, limiting the technology from widespread industrial applications [62]. Currently, the LPBF process is mainly used to produce high-value products for biomedical and engineering applications

in the aerospace and automobile industries [16]. These industries require a specific surface quality for a specific application. For example, in the biomedical industry implanted medical devices are in direct contact with the host tissues [2,63]. The surface quality of the implanted devices (dental implants, knee implants, hip implants etc.) influences the bone anchoring process. Therefore, a specific high-quality surface finish is required to ensure an effective healing process [2,63].

To improve the surface quality of the layers, a rescanning strategy was employed. It was observed that the surface roughness, R_z , of the layers reduced with almost about 40% after the rescanning strategy as shown in Figure 11. During the first exposure of the laser powder bed, the uneven track heights (Figs. 6 and 7) of the fused tracks forming the layers could lead to asymmetry in the cross-section of tracks. The denudation effect could also lead to a non-uniform thickness of the fused layers (Fig. 12). These phenomena could lead to varied powder material volume utilisation in the formation of subsequent tracks, from scan to scan (see Fig. 12) [34].

During the rescan exposure of the powder bed, the thermophysical conditions of the powder bed is different due to a stochastic exposure strategy in line with the "island principle" [64]. After the first exposure, the molten pool solidified and formed islands (satellites) of repeated solidification lines on the Ti10Mo alloy matrix surface. According to the island principle [64], the absorptivity of surfaces increases with increasing surface roughness. The solidified islands had increased the absorption of the laser radiation by the powder bed resulting in an increase in the operating temperature of the molten pool. The higher temperature of the molten pool increased the liquid phase of the molten pool leading to more prominent flow (stirring effect) [65]. Due to the stirring effect, the satellites were melted and incorporated into the bulk material resulting in improvement of the surface quality of the layers after the rescanning strategy. In the LPBF process, during the first exposure of the powder bed, the laser beam shifted in the plane of the fused tracks according to the selected hatch distances (80 μm, 90 μm, 100 μm) to form the layer. During the rescanning stage, the laser beam passed in between fused tracks and remelted every two neighbouring tracks. For the current experiment, the laser spot was set to move at 50% offset of the hatch distance. Thus, for 80 μm hatch distance the laser moved 40 μm before rescanning and for 90 μm and 100 μm it moved 45 μm and 50 μm, respectively, before rescanning.

Molybdenum has a higher melting point ($Mo = 2623^\circ C$, $Ti = 1668^\circ C$) and higher density ($Mo = 10,220 \text{ kg m}^{-3}$, $Ti = 4500 \text{ kg m}^{-3}$) than Ti [59]. Additionally, the laser reflectance of Mo is higher than that of Ti [66]. Due to these thermophysical differences, Ti powder particles would melt first, and the Mo powder particles would be displaced to the bottom of the molten pool. During the convective melt flow, Mo powder particles would be pushed to the periphery of the molten pool (pushing effect) [67]. The 50% offset of the hatch distances strategy employed during the rescanning stage ensured that the Mo powder particles that were pushed to the edge of the molten pool could be melted during the rescanning stage. As a result, it was observed

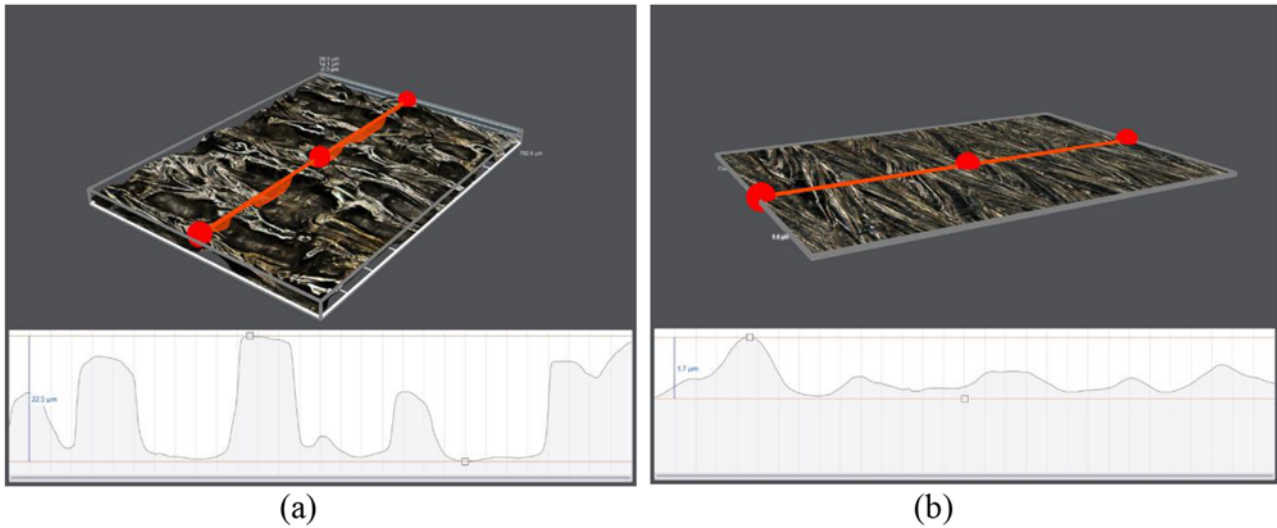


Fig. 12. Graphical representation of variation of the fused layer thickness from scan to scan, (a) Single scan (b) Rescan.

that the surface roughness of the layers after the rescanning stage improved (Figs. 11 and 12). Almost all the satellites melted completely, and the surface quality of the layers improved greatly.

Nonetheless, there were still pockets of Mo concentration (Tab. 2, Rescan layers. The white thin concentrations inside the red dotted ovals.) at the periphery of the molten pool due to the pushing effect, the rapid rate of the solidification front and the capturing of Mo in the rapid solidification front due to the high density of Mo (the slow-moving velocity of Mo in the Ti10Mo molten pool). These findings indicated that in situ alloying via the LPBF process still lacks the capacity to produce a “complete” homogenous alloy matrix as compared to pre-alloyed powders, which are still the principal feedstock used for the LPBF process. However, compared to most previous research results [10,38,68,69], the current investigation has shown great improvement of the melting of the Mo powder particles and homogeneity of the Ti-Mo alloy manufacturing through in-situ alloying. A thorough search of the literature revealed that in all the previous studies [10,38,68,69] it was not possible to melt the Mo powder particles completely via in-situ alloying using the LPBF manufacturing process. This was due to the larger size (20–45 μm) of the Mo powder particles used in all the previous research. A simulation conducted by Dzogbewu et al. [38] paved the way for possible manufacturing of the Ti- x Mo alloys without unmelted Mo powder particles. The simulation results of Dzogbewu et al. [38] revealed that using Mo powder particles with size $<20 \mu\text{m}$ could lead to the production of Ti- x Mo alloys without unmelted Mo powder particles. In the current research, the $1.0 \mu\text{m}$ Mo powder particles melted completely and the homogeneity of the Ti10Mo alloy also improved considerably. The steps taken in the current research (using Mo of $1.0 \mu\text{m}$ particle size and 50% offset rescanning strategy) opened a window of possibility of producing high-value products with the required surface quality in one manufacturing cycle. Such an approach would eliminate post-processing activities in

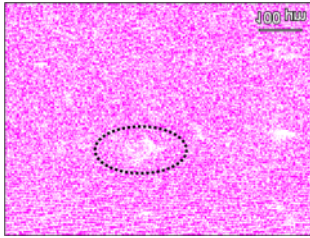
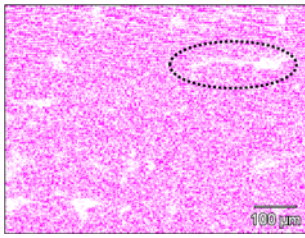
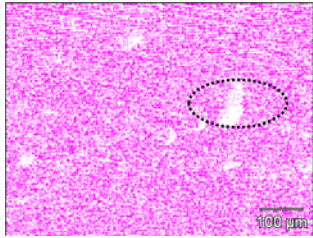
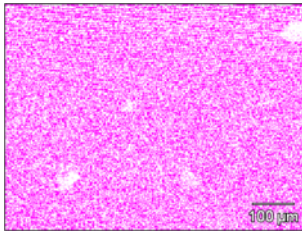
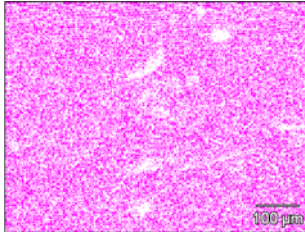
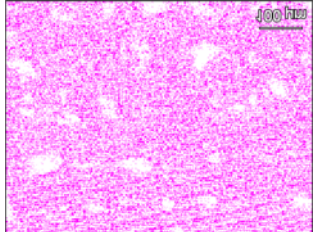
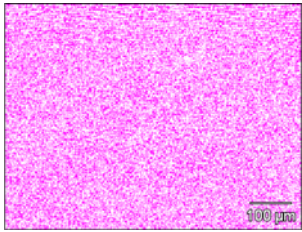
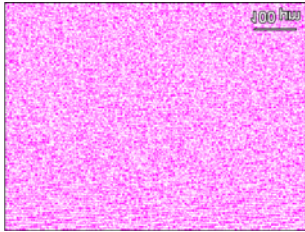
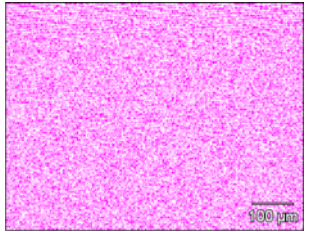
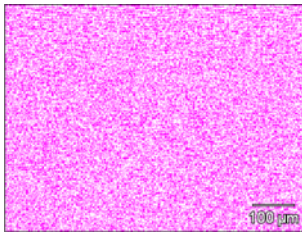
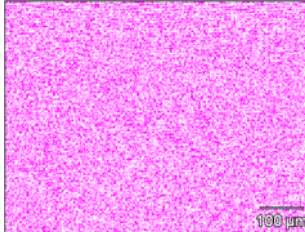
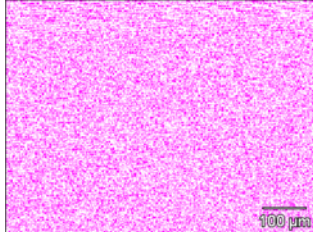
terms of improving the surface quality through blasting, polishing, etc. after the manufacturing process [70]. This would also improve the lead time advantage of the LPBF process as compared to the conventional manufacturing processes [6].

3.3.2 Elemental mapping

Since the fused tracks and layers were produced using an elemental powder blend of Ti and Mo, energy dispersive X-ray spectroscopy (EDS) elemental mapping was conducted to determine the degree of homogeneity of the Ti10Mo alloy matrix. It was observed that the elemental distribution of Mo in the Ti10Mo alloy matrix was not homogenous after the single exposure of the powder bed (Tab. 3–Single scan). Pockets of Mo concentration could be observed on the surfaces of the Ti10Mo layers (Tab. 3, the white spots inside the black dotted circles). Due to the high density of Mo powder particles, its velocity of movement is slower than that of the solidification rate of the molten pool [71]. Due to the inherent high solidification rate of the LPBF process [39], pockets of Mo were captured by the solidification front before the Mo could be homogeneously distributed in the Ti10Mo alloy molten pool. However, after the top surface of the layers were rescanned to homogenise the alloy (Tab. 3, the rescan layers), a great improvement in the homogeneity of the alloy after the 50% offset rescanning strategy was observed.

As already explained, the laser-matter interaction of the powder bed during the rescanning strategy is different from the first exposure of the powder bed. During the second exposure of the powder bed, there was no powder delivered onto the surface of the already solidified layer. Consequently, the thermo-physical conditions (absorptivity, reflectivity, thermal conductivity, heat transfer) of the solidified layer was completely different. Solidified islands formed during the single exposure increased the laser absorption of the layers. The higher operating temperature of the molten pool triggered the easy flowing of the molten

Table 3. Elemental mapping of the fused layers after single scanning and rescanning.

Process parameters	Single scan		
	80 μm	90 μm	100 μm
100 W, 0.5 m/s			
200 W, 1.0 m/s			
	Rescan		
100 W, 0.5 m/s			
200 W, 1.0 m/s			

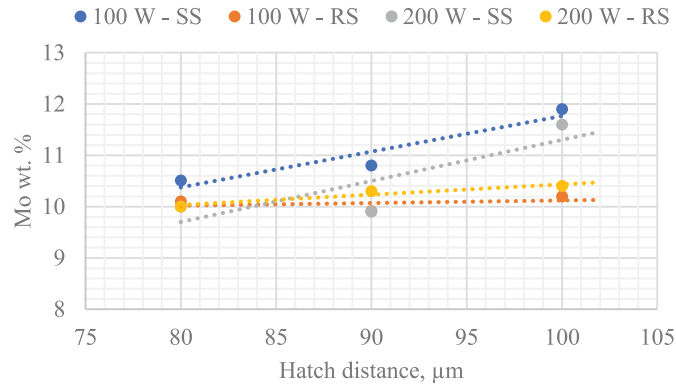


Fig. 13. Elemental homogeneity of the layers.

Table 4. Cross-sectional view of the layers.

Process parameters	Single scan		
	80 μm	90 μm	100 μm
150 W, 1.4 m/s			
200 W, 1.0 m/s			
	Rescan		
150 W, 1.4 m/s			
200 W, 1.0 m/s			

metal with a large liquid surface (stirring effect), which lead to the improvement in the homogeneity of the Ti10Mo alloy layers. Although it is generally reported that a rescanning strategy improves the homogeneity of the alloy matrix, it can be stated that the unique strategy of a 50% offset of the hatch distances has contributed considerably to the homogeneity of the alloy matrix.

3.3.3 Elemental homogeneity of the layers

The elemental concentration of Mo on the surfaces of the Ti10Mo layers was also investigated to determine the

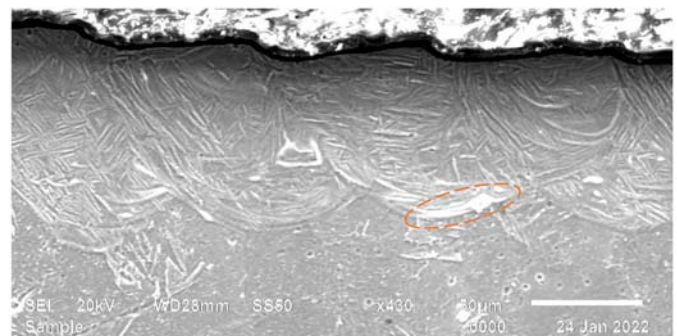


Fig. 14. A representative SEM image of the cross-sectional view.

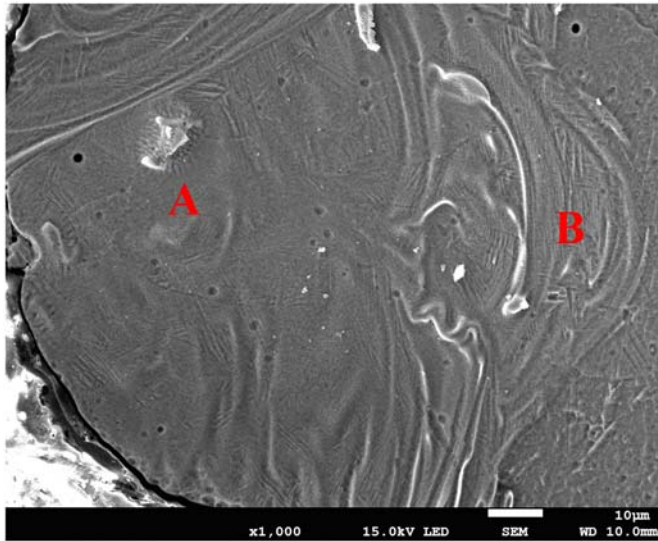


Fig. 15. Modes of solidification in the Ti10Mo.

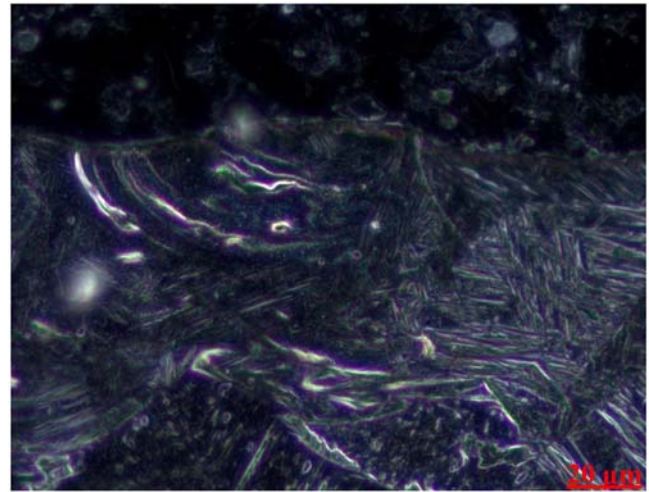


Fig. 16. Microstructure of Ti10Mo alloy matrix.

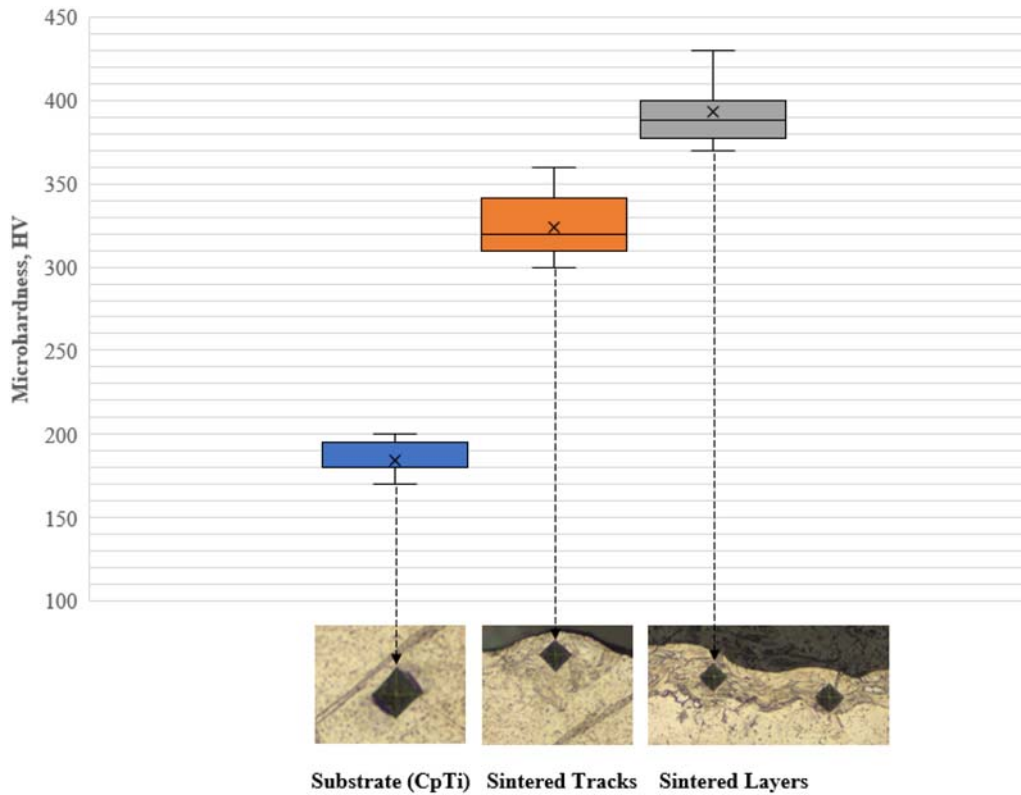


Fig. 17. Vickers microhardness value of Cp Ti, fused tracks and layers.

chemical homogeneity of Mo in the alloy matrix. As observed previously, the elemental composition of Mo in the Ti10Mo alloy matrix was inhomogeneous and increased with increasing hatch distance as displayed in Figure 13. After the rescanning process, the chemical homogeneity of Mo in the Ti10Mo alloy matrix improved, due to the prominent flow and the unique rescanning strategy employed.

3.3.4 Cross-sectional view of the fused layers

The cross-sections of the layers were also examined and are shown in Table 4. It was clear that all the layers overlapped perfectly without interlayer pores (gaps). Due to the occurrence of intense vortex flows in the molten pool, the solidified molten pool formed a wavier-like shape. The

vortex flow caused Mo to be distributed in the Ti10Mo alloy matrix with regions of concentrated Mo (Fig. 14, the orange dotted oval), just as observed from the top view. The effect of the rescanning strategy seemed not to have had a significant effect on the layers when observed on the cross-sections. Contrary to what was reported in most of the previous studies on the rescanning strategy, namely that the laser beam penetrated deep into the substrate due to the increase in absorption of the laser beam [36,53], no similar conspicuous observations were made in the current study. This could be due to the double layers used in the current study. Most of the previous authors used only a single layer to determine the optimum hatch distance [25,26]. For a single layer production, the layer (first layer) is fused on a substrate (plate) with lower surface roughness $<10\ \mu\text{m}$, whereas the second layer is synthesised on a layer with a higher surface roughness (Figs. 11 and 12) due to the vortex in the molten pool that produces uneven track heights (Figs. 6 and 7). Hence, using the double layer for the current investigation gave a more accurate approach of determining the optimum process parameters that could be used to produce a 3D object with structural integrity.

3.3.5 Solidification front and microstructure

Due to the layer wise building process, heat is extracted from the molten pool to the already solidified layers (thermal recycling) [39]. For pure metals, the extraction of the thermal energy from the molten pool leads to stabilization of the solidification front. However, due to solute redistribution which occurs in alloys, the extraction of the heat from the molten pool causes destabilization of the solidification front. The destabilisation of the solidification front occurs as a result of constitutional undercooling, causing the solidification front to switch from a planar to a cellular or dendritic solidification mode [68]. For the current study, the solidification mode of the Ti10Mo alloy was predominantly cellular as shown in Area B of Figure 15, with regions of planar mode shown in Area A of Figure 15. Although it is very rare for alloys to exhibit planar mode solidification, for the Ti10Mo constituent, as the laser beam traversed the powder bed, the concentration gradients of Mo in the molten pool at the liquid–solid interface was still increasing and had not reached a steady state. The initial lower solute of Mo in the Ti10Mo molten pool resulted in solidification of a stable planar front (Fig. 15–area A). As the LPBF process continued the concentration gradient of Mo in the molten pool increased and the molten front switched from planar mode to cellular mode. However, since Ti10Mo is not a pure metal, the solidification front consisted of predominantly cellular mode (Fig. 15–area B), indicating that the 10 wt.% Mo destabilised the solidification and caused the mode of solidification to transition from planar mode to cellular mode. It was the switching of the solidification front, thermal recycling, and epitaxial growth during the LPBF process that resulted in heterogeneous microstructures and subsequent variation in the mechanical properties of the LPBF manufactured components.

The Ti10Mo microstructure presented three distinct features (see Fig. 16): the α and β lamellar structure showing

a dark-grey varying contrast, pockets of Mo concentration (the bright whitish contrast) and acicular martensite phase. The martensitic (needle-like structures) features of the microstructure corresponded to the microstructure of LPBF bulk components due to the high rate of heating and cooling. The cooling velocity during the LPBF process is reported to be greater than $10^6\ \text{K s}^{-1}$ by Scipioni et al. [72], while the thermal gradient is estimated at $10^4\ \text{K mm}^{-1}$ by Shi et al. [73]. The high rate of melting and solidification leads to the needle-like structure of the microstructure.

3.3.6 Microhardness

The microhardness values of the fused tracks and layers were different, as shown in Figure 17. Theoretically, the microhardness of the fused tracks and layers should be in the same range. However, the fused tracks were directly on the substrate and the pyramid-shaped diamond indenter of the FM-700 Digital Vickers Microhardness Tester used for the study, indented through the track into the substrate, since the tracks were approximately $50\ \mu\text{m}$ high (powder layer thickness). Thus, the microhardness value of the substrate interfered with the microhardness value of the track, despite all the precautions taken to measure only the microhardness of the track. A stricter experimental design is required to be able to measure only the microhardness value of the track, excluding the substrate. For both the fused tracks and the layers, the values were dispersed. This could be due to the different solidification modes present. If the microhardness test was conducted in a planar area, a lower value was obtained, whereas if it was conducted in cellular solidified areas, a higher value was recorded. This observation synchronised with what is normally reported for LPBF products due to directional heat flux and the large thermal gradient [39]. The microhardness values obtained in the current experiment (Fig. 17) are within the range of what is reported in literature for Ti10Mo bulk samples. Chen et al. [1] reported microhardness values ranging from 381 to 451 HV for Ti10Mo bulk samples manufactured using a commercial arc-melting vacuum-pressure casting system. Syarif et al. [74] reported 410–430 HV for Ti9.8Mo samples. Collins et al. [75] used the laser engineered net-shaping (LENSTM) technology to produce Ti- x Mo alloys ($X=0-25\ \text{wt.}\%$) and reported a microhardness of 450 HV for a Ti10Mo composition.

4 Conclusion

The current research successfully determined the optimal process parameters that could be used to manufacture a Ti10Mo binary alloy without unmelted Mo particles and with improved homogenous microstructure via the LPBF process. The following conclusions were drawn from the study:

- Apart from thermophysical properties, powder particle size has a decisive effect on the melting and homogeneity of alloys during the LPBF in-situ alloying process.
- The complete melting of the Mo powder particles in the Ti10Mo powder blend was due to the small Mo powder particle size. Achieving complete melting of Mo via in-situ alloying opens a window of possibility of in-situ

alloying different refractory elements for specific applications.

- The 50% offset hatch distance rescanning strategy, uniquely employed in the current study, demonstrated that this unique rescanning strategy could improve the surface quality of LPBF samples by more than 40%.
- Based on the microstructure and microhardness values obtained, it was proven that single tracks and double layers could be used to predict the mechanical properties of LPBF built 3D components.
- The deviation of some process parameters from the normalised enthalpy theory attested to the non-linear behaviour of the LPBF process and also the importance of using more than one theory when verifying a phenomenon.
- Ti10Mo 3D components can be produced using laser powers of 150 W and 200 W at corresponding scanning speeds of 0.5 m/s and 1.0 m/s, respectively, with 80 μm hatch distance.

Data availability

The raw/processed data required to reproduce these findings can be shared on request.

Declaration of interests

The authors declare that they have no known competing financial interests or personal relationships that could have influenced the work reported in this paper.

Acknowledgements. This research was funded by the Collaborative Program in Additive Manufacturing (Contract No. CSIR-NLC-CPAM-21-MOA-CUT-01).

References

1. Y.Y. Chen, L.J. Xu, Z.G. Liu, F.T. Kong, Z.Y. Chen, Microstructures and properties of titanium alloys Ti-Mo for dental use, *Trans. Nonferrous Met. Soc. China (English Ed.)* **16** (2006) s824–s828
2. T.C. Dzogbewu, Additive manufacturing of porous Ti-based alloys for biomedical applications – a review, *J. New Gener. Sci.* **15** (2017) 278–294
3. M. Geetha, A.K. Singh, R. Asokamani, A.K. Gogia, Ti based biomaterials, the ultimate choice for orthopaedic implants – a review, *Progr. Mater. Sci.* **54** (2009) 397–425
4. T.C. Dzogbewu, Laser powder bed fusion of Ti6Al4V lattice structures and their applications, *J. Met. Mater. Miner.* **30** (2020) 68–78
5. M. Niinomi, Recent research and development in titanium alloys for biomedical applications and healthcare goods, *Sci. Technol. Adv. Mater.* **4** (2003) 445–454
6. T.C. Dzogbewu, S. Afrifa Jnr, N. Amoah, S.K. Fianko, D. de Beer, Additive Manufacturing Interventions during the COVID-19 Pandemic: South Africa, *Appl. Sci.* **12** (2021) 295
7. M. Niinomi, Y. Liu, M. Nakai, H. Liu, H. Li, Biomedical titanium alloys with Young's moduli close to that of cortical bone, *Regener. Biomater.* **3** (2016) 173–185
8. H. Liu, M. Niinomi, M. Nakai, J. Hieda, K. Cho, Changeable Young's modulus with large elongation-to-failure in β -type titanium alloys for spinal fixation applications, *Scr. Mater.* **82** (2014) 29–32
9. F.H. Sam Froes, Titanium for medical and dental applications – an introduction, in *Titanium in Medical and Dental Applications*, Elsevier (2018) pp. 3–21
10. T.C. Dzogbewu, Laser powder bed fusion of Ti15Mo, *Results Eng.* **7** (2020) 100155
11. M.L. Lourenço, G.C. Cardoso, K. dos S.J. Sousa, T.A.G. Donato, F.M.L. Pontes, C.R. Grandini, Development of novel Ti-Mo-Mn alloys for biomedical applications, *Sci. Rep.* **10** (2020) 1–8
12. W.F. Ho, C.P. Ju, J.H. Chern Lin, Structure and properties of cast binary Ti-Mo alloys, *Biomaterials* **20** (1999) 2115–2122
13. Y. Zhan, C. Li, W. Jiang, β -type Ti-10Mo-1.25Si-xZr biomaterials for applications in hard tissue replacements, *Mater. Sci. Eng. C* **32** (2012) 1664–1668
14. L.J. Xu, Y.Y. Chen, Z.G. Liu, F.T. Kong, The microstructure and properties of Ti-Mo-Nb alloys for biomedical application, *J. Alloys Compd.* **453** (2008) 320–324
15. C. Li, Y. Zhan, W. Jiang, β -Type Ti-Mo-Si ternary alloys designed for biomedical applications, *Mater. Des.* **34** (2012) 479–482
16. T.C. Dzogbewu, W.B. du Preez, Additive manufacturing of ti-based intermetallic alloys: a review and conceptualization of a next-generation machine, *Materials* **14** (2021) 4317
17. T.C. Dzogbewu, Additive manufacturing of TiAl-based alloys, *Manufactur. Rev.* **7** (2020) 35
18. S.A. Raji, A.P.I. Popoola, S.L. Pityana, O.M. Popoola, Characteristic effects of alloying elements on β solidifying titanium aluminides: a review, *Heliyon* **6** (2020) e04463
19. V.R. Jablovkov, M.J. Nutt, M.E. Richelsoph, H.L. Freese, The application of Ti-15Mo beta titanium alloy in high strength structural orthopaedic applications, *J. ASTM Int.* **2** (2005) 491–508
20. A. Vafadar, F. Guzzomi, A. Rassau, K. Hayward, Advances in metal additive manufacturing: a review of common processes, industrial applications, and current challenges, *Appl. Sci.* **11** (2021) 1–33
21. S. Mirzababaei, S. Pasebani, A review on binder jet additive manufacturing of 316L stainless steel, *J. Manufactur. Mater. Process.* **3** (2019) 82
22. T.C. Dzogbewu, N. Amoah, S.K. Fianko, S. Afrifa, D. de Beer, Additive manufacturing towards product production: a bibliometric analysis, *Manuf. Rev.* **9** (2022) doi: [10.1051/mfreview/2021032](https://doi.org/10.1051/mfreview/2021032)
23. T.C. Dzogbewu, W.B. du Preez, Additive manufacturing of titanium-based implants with metal-based antimicrobial agents, *Metals* **11** (2021) 1–12
24. T.C. Dzogbewu, L. Monaheng, I. Yadroitsava, W.B. du Preez, I. Yadroitsev, Finite element analysis in design of DMLS mandible implants, in *Challenges for Technology Innovation: An Agenda for the Future* (CRC Press/Balkema, 2017), pp. 155–160
25. A. Zenani, T.C. Dzogbewu, W.B. du Preez, I. Yadroitsev, Optimum process parameters for direct metal laser fusing of Ti6Al powder blend, *Univers. J. Mech. Eng.* **8** (2020) 170–182
26. L.A. Ramosena, B.S. Parker, T.C. Dzogbewu, W.B. du Preez, D.C. Blaine, Optimum process parameters for DMLS in-situ alloying of a Ti-10(60Al40V) powder blend, in *Rapid Product Development Association of South Africa (RAP-*

- DASA), 2019, pp. 78–93. Available: https://www.researchgate.net/publication/341343460_OPTIMUM_PROCESS_PARAMETERS_FOR_DMLS_IN-SITU_ALLOYING_OF_A_Ti-1060AL40V_POWDER_BLEND
27. O.M. Ivashishin, V.M. Anokhin, A.N. Demidik, D.G. Sawakin, Cost-effective blended elemental powder metallurgy of titanium alloys for transportation application, *Key Eng. Mater.* **188** (2000) 55–62
 28. M.A. Ilani, M. Khoshnevisan, Powder mixed-electrical discharge machining (EDM) with the electrode made by fused deposition modeling (FDM) at Ti-6Al-4V machining procedure, *Multiscale Multidiscip. Model. Exp. Des.* **3** (2020) 173–186
 29. N.H. Phan, V.N.Pi. S. Shirguppikar, M.S. Patil, M.A. Ilani, L.X. Hung, T. Muthuramalingam, T.Q. Hung et al., Material removal rate in electric discharge machining with aluminum tool electrode for Ti-6Al-4V titanium alloy, in *Lecture Notes in Networks and Systems 178* (Springer Science and Business Media Deutschland GmbH, 2021), pp. 527–533
 30. R. Ali Mahdavejad, M. Asghari Ilani, Superior advance research in the electro-discharge machining of Ti alloys: review, *Int. J. Sci. Res. Mech. Mater. Eng.* (2019) 19–38
 31. N. Khanna, K. Zadafiya, T. Patel, Y. Kaynak, R.A. Rahman Rashid, A. Vafadar, Review on machining of additively manufactured nickel and titanium alloys, *J. Mater. Res. Technol.* **15** (2021) 3192–3221
 32. M. Losertová, V. Kubeš, Microstructure and mechanical properties of selective laser melted Ti6Al4V alloy, *IOP Conf. Ser.: Mater. Sci. Eng.* **266** (2017) 012009
 33. T.G. Spears, S.A. Gold, In-process sensing in selective laser melting (SLM) additive manufacturing, *Integr. Mater. Manufactur. Innov.* **5** (2016) 16–40
 34. I. Yadroitsev, P. Krakhmalev, I. Yadroitsava, Hierarchical design principles of selective laser melting for high quality metallic objects, *Addit. Manuf.* **7** (2015) 45–56
 35. Struers, Metallographic preparation of powder metallurgy parts. Accessed: Feb. 05, 2022. Available: <https://www.struers.com/en/Knowledge/Materials/Powder-metallurgy>
 36. T.C. Dzogbewu, Laser powder bed fusion of Ti6Al4V-xCu: process parameters, *J. Met. Mater. Miner.* **31** (2021) 62–70
 37. S.A. Khairallah, A. Anderson, Mesoscopic simulation model of selective laser melting of stainless steel powder, *J. Mater. Process. Technol.* **214** (2014) 2627–2636
 38. T.C. Dzogbewu, I. Yadroitsev, P. Krakhmalev, I. Yadroitsava, A. du Plessis, Optimal process parameters for in situ alloyed Ti15Mo structures by laser powder bed fusion, in *Solid Freeform Fabrication 2017: Proceedings of the 28th Annual International Solid Freeform Fabrication Symposium – An Additive Manufacturing Conference, SFF 2017* (2020) pp. 75–96
 39. S.A. Khairallah, A.T. Anderson, A. Rubenchik, W.E. King, Laser powder-bed fusion additive manufacturing: physics of complex melt flow and formation mechanisms of pores, spatter, and denudation zones, *Acta Mater.* **108** (2016) 36–45
 40. S. Das, Physical aspects of process control in selective laser fusing of metals, *Adv. Eng. Mater.* **5** (2003) 701–711
 41. C. Körner, E. Attar, P. Heintl, Mesoscopic simulation of selective beam melting processes, *J. Mater. Process. Technol.* **211** (2011) 978–987
 42. T.C. Dzogbewu, W.B. du Preez, Producing Ti5Mo-fused tracks and layers via laser powder bed fusion, *Metals* **12** (2022) 950
 43. L. Rayleigh, XIX. On the instability of cylindrical fluid surfaces, *London, Edinburgh, Dublin Philos. Mag. J. Sci.* **34** (1892) 177–180
 44. S. Kou, C. Limmaneevichitr, P.S. Wei, Oscillatory marangoni flow: a fundamental study by conduction-mode laser spot welding, *Weld. J.* **90** (2011)
 45. L. Pekker, Plateau-Rayleigh Instability of a Cylinder of Viscous Liquid (Rayleigh vs. Chandrasekhar). Accessed: Aug. 19, 2021. [Online]. Available: <https://arxiv.org/abs/1712.07069v1>.
 46. P. Fischer, V. Romano, H.P. Weber, N.P. Karapatis, E. Boillat, R. Glardon, Fusing of commercially pure titanium powder with a Nd:YAG laser source, *Acta Mater.* **51** (2003) 1651–1662
 47. W. Liu, J.N. Dupont, Effects of substrate crystallographic orientations on crystal growth and microstructure development in laser surface-melted superalloy single crystals. Mathematical modeling of single-crystal growth in a melt pool (Part II), *Acta Mater.* **53** (2005) 1545–1558
 48. E. Saiz, A.P. Tomsia, R.M. Cannon, Ridging effects on wetting and spreading of liquids on solids, *Acta Mater.* **46** (1998) 2349–2361
 49. I. Yadroitsev, P. Krakhmalev, I. Yadroitsava, S. Johansson, I. Smurov, Energy input effect on morphology and microstructure of selective laser melting single track from metallic powder, *J. Mater. Process. Technol.* **213** (2013) 606–613
 50. R. Prümmer, History of shock waves, explosions and impact – a chronological and biographical reference, *Peter O.K. Krehl, Propellants, Explos. Pyrotech.* **34** (2009) 458–458
 51. K.A. Mumtaz, N. Hopkinson, Selective laser melting of thin wall parts using pulse shaping, *J. Mater. Process. Technol.* **210** (2010) 279–287
 52. I. Yadroitsev, Selective laser melting: Direct manufacturing of 3D-objects by selective laser melting of metal powders, *Appl. Catal. B Environ.* **75** (2009) 229–238
 53. A. Kinnear, T.C. Dzogbewu, P. Krakhmalev, I. Yadroitsava, I. Yadroitsev, Manufacturing, microstructure and mechanical properties of selective laser melted Ti6Al4V-Cu, in *Proceedings of the LiM- Lasers in Manufacturing, World of Photonics Congress, München, Germany, 25–29 June, 2017* (2017)
 54. C. Qiu, C. Panwisawas, M. Ward, H.C. Basoalto, J.W. Brooks, M.M. Attallah, On the role of melt flow into the surface structure and porosity development during selective laser melting, *Acta Mater.* **96** (2015) 72–79
 55. W.E. King et al., Observation of keyhole-mode laser melting in laser powder-bed fusion additive manufacturing, *J. Mater. Process. Technol.* **214** (2014) 2915–2925
 56. J. Yang et al., Role of molten pool mode on formability, microstructure and mechanical properties of selective laser melted Ti-6Al-4V alloy, *Mater. Des.* **110** (2016) 558–570
 57. R. Rai, J.W. Elmer, T.A. Palmer, T. Debroy, Heat transfer and fluid flow during keyhole mode laser welding of tantalum, Ti-6Al-4V, 304L stainless steel and vanadium, *J. Phys. D: Appl. Phys.* **40** (2007) 5753–5766
 58. D. Bäuerle, *Laser Processing and Chemistry* (Springer, Berlin, Heidelberg, 2011)
 59. AZoM, Titanium Alloys - Physical Properties, AZO Materials (2002). <https://www.azom.com/article.aspx?ArticleID=1341> (accessed Aug. 19, 2021)
 60. Y. Shi et al., Metal materials for additive manufacturing, *Mater. Addit. Manuf.* (2021) 403–595

61. T.C. Dzogbewu, Y.D. Arthur, Comparative studies of locally produced and imported low-carbon steels on the Ghanaian market, *J. Nat. Sci.* **1** (2013) 15–22
62. E. Yasa, O. Poyraz, E.U. Solakoglu, G. Akbulut, S. Oren, A study on the stair stepping effect in direct metal laser fusing of a nickel-based superalloy, *Proc. CIRP* **45** (2016) 175–178
63. N. Nhlapo, T.C. Dzogbewu, O. de Smidt, A systematic review on improving the biocompatibility of titanium implants using nanoparticles, *Manuf. Rev.* **7** (2020) 31
64. D. Bergström, J. Powell, A.F.H. Kaplan, A ray-tracing analysis of the absorption of light by smooth and rough metal surfaces, *J. Appl. Phys.* **101** (2007) doi: [10.1063/1.2738417](https://doi.org/10.1063/1.2738417)
65. K. Arafune, A. Hirata, Thermal and solutal Marangoni convection in In-Ga-Sb system, *J. Cryst. Growth* **197** (1999) 811–817
66. E.D. Palik, *Handbook of optical constants of solids 1* (Elsevier, 2012)
67. J.Q. Xu, L.Y. Chen, H. Choi, X.C. Li, Theoretical study and pathways for nanoparticle capture during solidification of metal melt, *J. Phys. Condens. Matter* **24** (2012)
68. B. Vrancken, L. Thijs, J.P. Kruth, J. Van Humbeeck, Microstructure and mechanical properties of a novel β titanium metallic composite by selective laser melting, *Acta Mater.* **68** (2014) 150–158
69. F. Huber, M. Rasch, M. Schmidt, Laser powder bed fusion (Pbf-lb/m) process strategies for in-situ alloy formation with high-melting elements, *Metals (Basel)*. **11** (2021) 1–15
70. G.A. Longhitanoa, M.A. Larosaa, A.L.J. Munhoza, C.A. De Carvalho Zavagliaa, M.C.F. Ierardia, Surface finishes for Ti-6Al-4V alloy produced by direct metal laser sintering, *Mater. Res.* **18** (2015) 838–842
71. L. Hadji, Morphological instability prior to particle engulfment by a solidifying interface, *Scr. Mater.* **48** (2003) 665–669
72. U. Scipioni Bertoli, G. Guss, S. Wu, M.J. Matthews, J.M. Schoenung, In situ characterization of laser-powder interaction and cooling rates through high-speed imaging of powder bed fusion, *Additive Manufactur.* **135** (2017) 385–396
73. Q. Shi, D. Gu, M. Xia, S. Cao, T. Rong, Effects of laser processing parameters on thermal behavior and melting/solidification mechanism during selective laser melting of TiC/Inconel 718 composites, *Opt. Laser Technol.* **84** (2016) 9–22
74. J. Syarif, T.N. Rohmannudin, M.Z. Omar, Z. Sajuri, S. Harjanto, Stability of the beta phase in Ti-Mo-Cr alloy fabricated by powder metallurgy, *J. Min. Metall. Sect. B Metall.* **49** (2013) 285–292
75. P.C. Collins, R. Banerjee, S. Banerjee, H.L. Fraser, Laser deposition of compositionally graded titanium-vanadium and titanium-molybdenum alloys, *Mater. Sci. Eng. A* **352** (2003) 118–128

Cite this article as: Thywill Cephas Dzogbewu, Willie Bouwer du Preez, In situ alloying of Ti10Mo fused tracks and layers via laser powder bed fusion, *Manufacturing Rev.* **9**, 23 (2022)